Imaging the lowermost mantle (*D″*) and the core–mantle boundary with *SKKS* coda waves

Ping Wang,[1] Maarten V. de Hoop[1,2] and Robert D. van der Hilst[1]

[1]*Department of Earth, Atmospheric, and Planetary Sciences, Massachusetts Institute of Technology, Cambridge MA* 02139, *USA. E-mail: wango@mit.edu*
[2]*Center for Computational and Applied Mathematics, Purdue University,* 150 *N. University Street, West Lafayette IN* 47907, *USA*

SUMMARY
In our previous studies we developed a method for imaging heterogeneity at and near the core–mantle boundary (CMB) with a generalized Radon transform (GRT) of (transverse component, broad-band) *ScS* data, and we developed a statistical model for producing images of the *D″* discontinuity with variable confidence levels. In these applications, the background is smooth and perturbations are represented as contrasts. Here we extend the theory to allow (known) discontinuities, such as the CMB, in the background model. The resulting imaging operator, which is formally not a GRT, can be used, either alone or along with *ScS*, for the imaging of lowermost mantle structure and, in particular, the *D″* discontinuity with the scattered SKKS wavefield. Synthetic seismograms calculated with the *WKBJ* method are used to test the performance of our approach. As a proof of concept, we transform ∼38 000 radial component *SKKS* waveforms into image gathers of a CMB patch beneath Central America. The *SKKS* image gathers and image traces are in good agreement with the image traces obtained from the GRT transform of *ScS* data.

Key words: Image processing; Wave scattering and diffraction.

1 INTRODUCTION

Transmission tomography has been very successful in mapping smooth variations in elastic properties in Earth's mantle (Van der Hilst *et al.* 1997; Romanowicz 2003). To detect heterogeneities in Earth's interior that are singular in nature, however, the use of scattered body wave phases is pertinent. The singular parts of these waves contain information about non-smooth variations in material and physical properties of the Earth. Seismological investigations of the structure of and near the core–mantle boundary (CMB) region used to rely mostly on forward modelling of waveforms of phases like *S-ScS* and *SKS-SPdKS-SKKS* on selected high-quality seismograms (Garnero 2000). To benefit more from the ever growing modern data sets, methods based on inverse scattering, such as basic Kirchhoff migration (Thomas *et al.* 2004; Hutko *et al.* 2006), have begun to be adopted from application in exploration seismology.

Albeit with different approximations and purposes, Wang *et al.* (2006) and Chambers & Woodhouse (2006) used the generalized Radon transform (GRT), first adopted for seismic imaging in the early 1980s (Beylkin 1984), to image selected neighbourhoods of the CMB using *ScS* data. In addition, Ma *et al.* (2007) developed a statistical method to enhance the GRT images of discontinuities and estimate their uncertainty. With this modified GRT approach, Van der Hilst *et al.* (2007) detected multiple, piecewise continuous interfaces in the *D″* region beneath Central America. Some of these are consistent with expectations from a perovskite to post-perovskite phase transformation, which increases the plausibility that such a transition does indeed occur at pressure and temperature conditions for the lowermost mantle.

GRT imaging with the *ScS* wavefield allows systematic, large scale imaging of the lowermost mantle in regions of adequate coverage. Examples include Central and North America (Wang *et al.* 2006; Van der Hilst *et al.* 2007) and SE Asia (work in preparation). Many other regions, such as the deep mantle beneath large ocean basins, are less amenable for GRT imaging with *ScS* waves. To put additional and independent constraints on *D″* structure, we develop here a method for imaging the lowermost mantle from below—that is, from the core side—with the *SKKS* wavefield (Fig. 1). The use of *SKKS* data has two main advantages. First, in areas well sampled by both *ScS* and *SKKS*, joint inversion of top and underside reflections will put superior constraints on lowermost mantle heterogeneity and, perhaps, anisotropy. Second, *SKKS* provides excellent data coverage of the CMB region over large areas, including those that are not adequately sampled—or not at all sampled—by *ScS* waves (Fig. 2).

The *SKKS* wavefield has been used in shear-wave splitting analysis (Clitheroe & Van der Hilst 1998), and phases such as *PKKP* can constrain CMB topography (Sze & van der Hilst 2003), but such phases are not normally considered for imaging of the lowermost mantle. Our original objective was to use inverse scattering with *SKKS* to scan the core-side of the CMB, but the realization that some of its energy
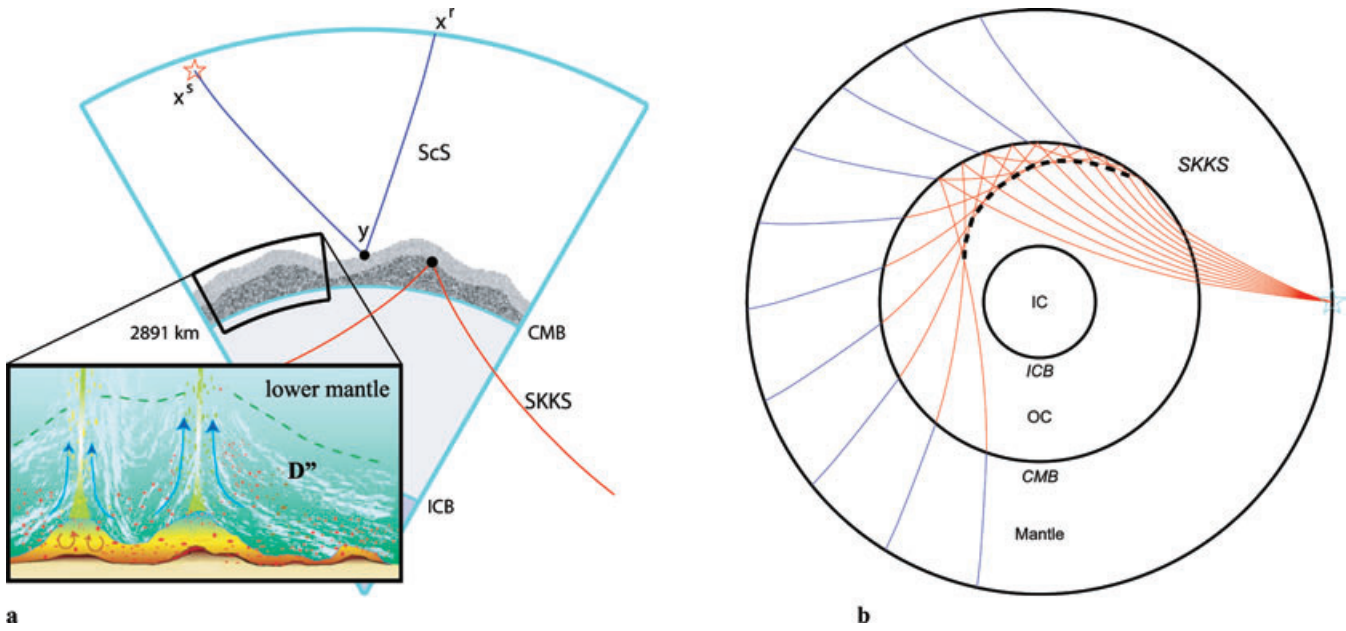
GJI Seismology

Figure 1. (a) *ScS* and *SKKS* ray geometry used for D'' high-resolution imaging of structures in the lowermost mantle, also referred to as D'' region, which may arise from boundary layer processes (e.g. flow), lateral variations in composition and pressure induced phase changes (as depicted in the inset, after Garnero 2000). (b) Generic ray geometry of *SKKS*. The dashed black line is where the phenomenon of a caustic occurs.
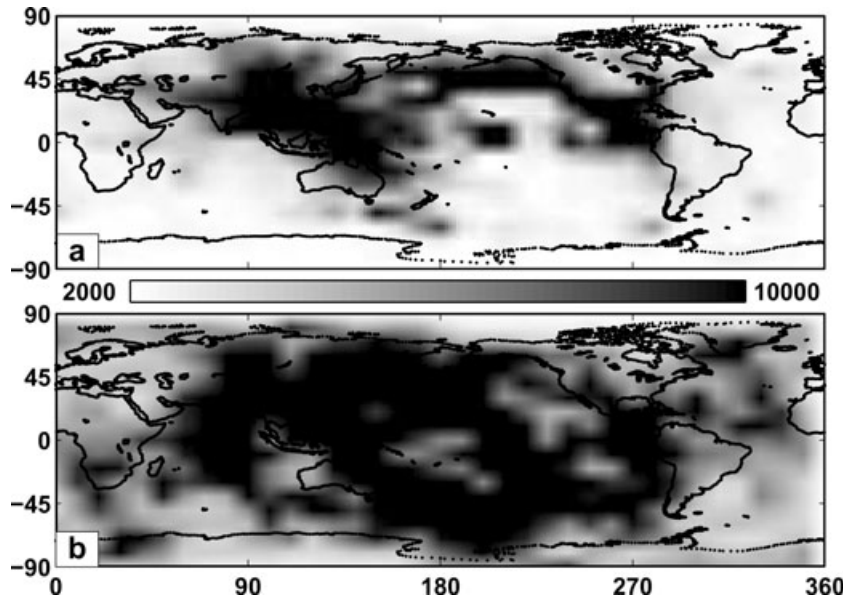

Figure 2. Contour maps of number of *ScS* (a) and *SKKS* (b) reflection points in $10° \times 10°$ bins at the core–mantle boundary. For the plots we used source–receiver combination for data that are available through IRIS-DMC ($m_b \geq 5.2$, 1988–2002, $\sim$3200 stations, $\sim$4000 events).

may scatter from structure just above the CMB inspired us to explore the possibility of using *SKKS* for lowermost-mantle imaging. In fact, Rost & Revenaugh (2004) observed a strong arrival in the early coda of major-arc *PKKPab* and used it to locate a D'' interface at $\sim$280 km above the CMB. Global energy stacks of *SKKS*(*SV*) reveal distinct arrivals in the coda of the main *SKKS* phase (see the black box in Fig. 3). Much of this energy may be associated with multiple reflections [$SK_N S$ ($N > 2$), for instance, $SKKKS = SK_3 S$], but some of it is associated with underside reflections from interfaces in the lower mantle (e.g. the top of the D'' layer).

The use of *SKKS* to image D'' from below faces several challenges. First, since *SKKS* traverses both through the solid mantle and the liquid outer core, one has to account for multiple solid-liquid crossings. Second, whereas for *ScS* we could use the relative simple system of transversely polarized (*SH*) waves, for *SKKS* imaging we need to consider the coupled *P*–*SV* system. Indeed, the potential mixture of SKS^dSKS and SKP^dPKS may seem to make this approach infeasible. Third, for the construction of an imaging operator based on single scattering there is—compared with the GRT of *ScS* data—the added complexity that the background model, relative to which perturbations
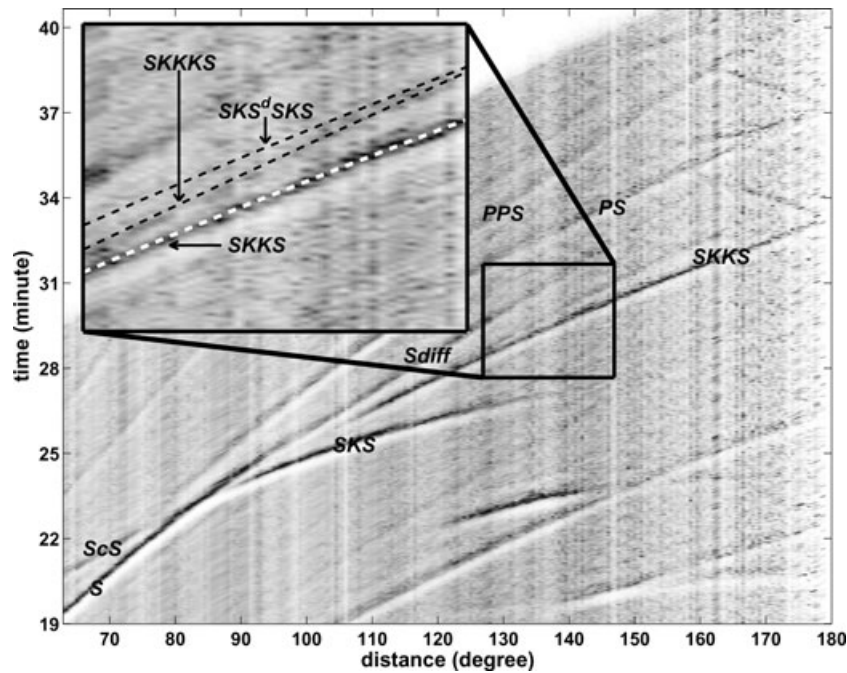
Figure 3. Stack of the ~165 000 global *SKKS*(*SV*) data. Processing details data source is IRIS-DMC, bandpass filter is 10–50 s and earthquakes have $m_b \geq 6.0$, with origin time between 1990 and 2007. In the blowup, the dashed black line is the theoretical traveltime curve for *SKKS*, the dotted red line is the traveltime curve for *SKKKS* and the dotted green line is the traveltime curve of *SKS^{d}SKS* for a *D″* 300 km above the CMB.

are sought (that is, elasticity contrasts in *D″*), is no longer smooth and must itself contain an interface (that is, the CMB). Fourth, the multiples SK_NS (where $N > 2$) arrive in the time window close to that of *SKS^{d}SKS*.

Fortunately, the propagation speeds in the outer core and lower mantle create favourable conditions for GRT-like imaging with *SKS^{d}SKS*. Because of the small wave speed contrast between outer core *K* and lower-mantle *S* speed, the change in propagation direction (from *K* to *S*) across the CMB and the effects of local CMB topography on ray geometry and traveltime of *SKS^{d}SKS* are also small. Instead of treating the multiple interactions of the *SKKS* wave with the CMB as a multiple scattering problem we, therefore, fix the CMB at a reference depth. Due to the non-smoothness of the background the imaging operator is formally not a GRT, but we can still treat it (and refer to it) as such. Furthermore, the large difference between core *K* and lower-mantle *P* wave speeds produces post-critical *P*-wave transmission into the mantle for all but the largest epicentral disctances for which *SKKS* data are available. This leaves a large epicentral distance range (100°–180°) in which there is no *SKP^{d}PKS* or *SKP^{d}SKS* energy (see Fig. 4). This is, in fact, a distinct advantage of *SKS^{d}SKS* over *PKP^{d}PKP*. Indeed, in the small epicentral distance range where *PKP^{d}PKP* exists—and could be used to locate *D″* (Rost & Revenaugh 2004)—converted *S* (for instance, *PKS^{d}SKP*), as well as triplications in the *PKKP* wavefield will add significant complexity to the observed radial component wavefield. Finally, we will demonstrate that the presence of multiples (that is, SK_NS, $N > 2$) waves is not a problem. Their slownesses are different from *SKKS* (and *SKS^{d}SKS*), and in the angle gathers they distinguish themselves through a clear residual moveout. Even without further processing, this prevents the multiples from contributing much to the slowness integrations, but we separate and suppress them using forward and inverse parabolic Radon transforms (Alvarez & Larner 2004).

The main goal of this paper is to develop a mixed fluid–solid imaging operator, which resembles a GRT, and apply it to image the *D″* beneath Central America with the broad-band, radial component *SKKS* wavefield. In Section 2, we develop the theory underlying the 'GRT' and describe how three-component broad-band data can be transformed into angle gathers. In Section 3, we use synthetic seismograms to test the performance of our methodology. We show that the multiples SK_NS can be suppressed and that the 'GRT' based on the *SKKS* phase can resolve interfaces in the lowermost mantle. Finally, in Section 4, we present results of the 'GRT' based on *SKKS* and compare them with results from GRT imaging with the *ScS* wavefield.

2 INVERSE SCATTERING OF *SKS^{d}SKS* WAVES

The GRT assumes single scattering (it uses the Born approximation) and considers perturbations (that is, contrasts) in elasticity with respect to a smooth background model. This formulation is adequate for *ScS* waves (Wang *et al.* 2006), but without modification it cannot be applied to the *SKKS* wavefield. Because of its multiple interactions with the (large) contrast in elastic properties between the (solid) mantle and (liquid) core associated with the CMB. The CMB is not, however, an imaging target. Moreover, the wave speed contrast between outer core *K* and lower mantle *S* is small, and thus the refraction index (for transmitted *S* waves) is close to 1. This permits the following simplification. Instead of considering the CMB (along with the scatter points above it) as a perturbation, which would produce a multiple scattering problem, we
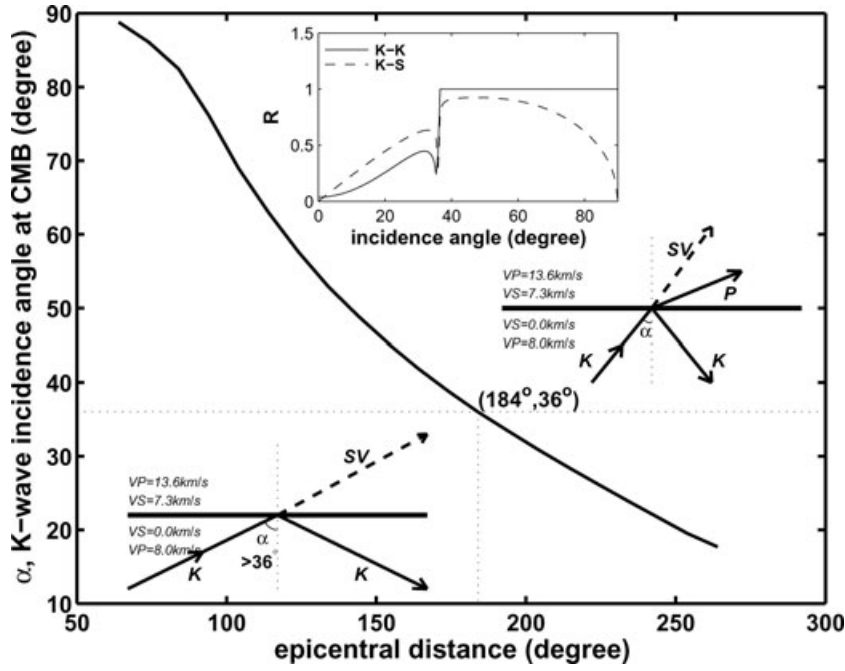
Figure 4. The *K*-wave incidence angle at the CMB versus the epicentral distance for the *SKKS* phase. The inset is the *K–K* reflection and *K–S* conversion coefficients versus the incidence angle at the CMB. For an epicentral distance $\Delta < 184°$, the *K*-wave incidence angle $\alpha > 36°$. $\alpha = 36°$ is the critical angle where the *K*-wave completely reflects, thus there is no *P*-wave energy in the mantle for an epicentral distance smaller than 184°. R represents the reflection/transmission coefficients: *K–K/K–S*.

include the CMB as a known interface in the background model and incorporate the wavefield interactions with it (by imposing the appropriate boundary conditions) in the unperturbed (reference) wavefield. The perturbed wavefield is then inverted for model perturbations (scatterers) above the CMB. The associated imaging operator is (strictly speaking) not a GRT because of the non-smoothness of the background, but for $SKS^d SKS$ waves it still belongs to the category of adjoint operators appearing in the lineralized least-squares inversion for singularities. Hereinafter we, therefore, refer to it, loosely, as a GRT.

In the subsections that follow, we develop the GRT-like operator by first introducing the Green's function and tensor for the governing equations in both fluid and solid media, followed by their ray-geometric (asymptotic) representations. We then incorporate the sources (using a far-field approximation) and the CMB in the background model. The effects of the CMB on the amplitudes are accounted for through the appropriate boundary conditions and through inclusion of the effects of CMB curvature on geometrical spreading. Finally, we develop the short-period Born approximation (Aki & Richards 1980) that models the $SKS^d SKS$ phases and obtain the associated linear scattering operator—in particular, its amplitude and phase function. At this point, the results of Wang *et al.* (2006) can be directly applied, subject to a modification of the relevant amplitudes and phases in the transition from topside *ScS* reflections to the underside $SKS^d SKS$ phases, to obtain the imaging operator or inverse scattering transform. The inverse scattering transform can, under certain conditions, be subjected to a restriction to a prescribed scattering angle and azimuth (θ, ψ). This produces common image point gathers, which represent multiple images of reflectivity at a chosen location in Earth's interior. Upon the construction of these gathers, we correct the traveltimes for mantle heterogeneity using a tomographic model for mantle *S*-wave speed due to Grand (2002).

2.1 The governing wave equations

In the solid regions of the Earth, like the mantle, the particle displacement with components $u_i = u_i(\mathbf{x}, t)$ satisfies the elastic wave equation

$$\rho \, \partial_t^2 u_i - \partial_j(c_{ijk\ell} \partial_\ell u_k) = f_i, \tag{1}$$

where $\rho = \rho(\mathbf{x})$ is the scalar mass density, $c_{ijk\ell} = c_{ijk\ell}(\mathbf{x})$ is the elastic stiffness tensor and $f_i = f_i(\mathbf{x}, t)$ is the body-force source density (Throughout, x_j denote the coordinates of $\mathbf{x}$). The stress τ_{ij} in the solid is related to the displacement as $\tau_{ij} = c_{ijk\ell} \partial_\ell u_k$, in accordance with Hooke's law. The elastodynamic Green's tensor, $G_{ip}(\mathbf{x}, \mathbf{x}', t)$, which is the solution of the wave equation for a point source operative at $(\mathbf{x}', t)$, satisfies the equation

$$\rho \, \partial_t^2 G_{ip} - \partial_j(c_{ijk\ell} \partial_\ell G_{kp}) = \delta_{ip}\delta(\mathbf{x} - \mathbf{x}')\delta(t), \tag{2}$$

subject to the condition of causality, $G_{ip}(\mathbf{x}, \mathbf{x}', t) = 0$ for $t < 0$. The modes of seismic wave propagation (in the mantle) are *P*, *SV* and *SH* in the isotropic case and *qP*, *qSV* and *qSH* in the anisotropic case considered.

In the fluid regions of the Earth, such as the outer core, the acoustic pressure perturbation, $p = p(\mathbf{x}, t)$, satisfies an acoustic wave equation

$$\chi\, \partial_t^2 p - \partial_j(\sigma \partial_j p) = q \,, \tag{3}$$

where $\sigma = \sigma(\mathbf{x}) = \rho_f(\mathbf{x})^{-1}$ is the scalar reciprocal density of mass, $\chi = \chi(\mathbf{x}) = \kappa(\mathbf{x})^{-1}$ is the compressibility or reciprocal of bulk modulus, $\kappa(\mathbf{x})$ and $q = q(\mathbf{x}, t)$ is the time derivative of the volume source density of injection rate. The scalar traction in the fluid is the opposite of the pressure; the particle velocity v_i in the fluid is related to the pressure as $v_i = -\rho^{-1}\partial_t^{-1}\partial_i p$. The acoustic Green's function, $G(\mathbf{x}, \mathbf{x}', t)$, satisfies the equation

$$\kappa\, \partial_t^2 G - \partial_j(\sigma \partial_j G) = \delta(\mathbf{x} - \mathbf{x}')\delta(t), \tag{4}$$

again subject to the condition of causality, $G(\mathbf{x}, \mathbf{x}', t) = 0$ for $t < 0$. The mode of (acoustic) seismic wave propagation in the outer core is denoted by K.

The frequency domain equations, both for the solid and the fluid regions, are obtained by replacing $-\mathrm{i}\partial_t$ by ω. At a solid–fluid interface, the following boundary conditions apply: (1) the normal component of the particle displacement is continuous; (2) the normal component of the surface traction in the solid and the scalar traction in the fluid are equal and (3) the tangential components of the surface traction in the solid vanish.

2.2 Geometrical-ray Green's tensors in fluids and solids

We first discuss the high-frequency Green's tensor in a solid region (that is, in the absence of a fluid region). Away from caustics at the receiver at $\mathbf{x}$ and the source at $\mathbf{x}'$, the Green's tensor is given by the oscillatory integral representation (5.4.24 Červený 2001)

$$G_{ip}(\mathbf{x}, \mathbf{x}', t) = \frac{1}{\pi} \sum_m \mathrm{Re} \int_0^\infty \xi_i(\mathbf{x})\xi_p(\mathbf{x}')A^{(m)}(\mathbf{x}, \mathbf{x}')\, \exp\{\mathrm{i}\omega\,[t - T^{(m)}(\mathbf{x}, \mathbf{x}')]\}\, \mathrm{d}\omega. \tag{5}$$

Here, $\boldsymbol{\xi}$ denotes the normalized polarization vector of the wave-type under consideration, $A^{(m)}(\mathbf{x}, \mathbf{x}')$ the amplitude and $T^{(m)}(\mathbf{x}, \mathbf{x}')$ the traveltime along the ray or path connecting $\mathbf{x}$ with $\mathbf{x}'$. The index m labels the traveltime branches and keeps track of multipathing, but where not strictly necessary, it will be suppressed in our notation. The amplitude is obtained from

$$A(\mathbf{x}, \mathbf{x}') = \frac{1}{4\pi\,[\rho(\mathbf{x})\rho(\mathbf{x}')\,\mathcal{M}(\mathbf{x}, \mathbf{x}')]^{1/2}}, \tag{6}$$

with

$$\mathcal{M}(\mathbf{x}, \mathbf{x}') = \|v(\mathbf{x}')\| V(\mathbf{x}) \frac{\partial(\mathbf{x}^{\mathrm{W}})}{\partial(\gamma^{\mathrm{O}})}, \tag{7}$$

upon multiplication by the phase factor $\exp\,[-\,\mathrm{i}\,(\pi/2)\,\iota(\mathbf{x}, \mathbf{x}')]$, which accounts for the KMAH index ι. In (7), v denotes the group velocity and V denotes the phase velocity (in the direction along the ray connecting $\mathbf{x}$ with $\mathbf{x}'$ according to branch m), $\mathbf{x}^{\mathrm{W}}$ denotes coordinates in the wave front at $\mathbf{x}$, and γ^{O} coordinates on the slowness surface at $\mathbf{x}'$. Also,

$$V(\mathbf{x}')\mathcal{R}(\mathbf{x}, \mathbf{x}') := \{\mathcal{M}(\mathbf{x}, \mathbf{x}')/[V(\mathbf{x})V(\mathbf{x}')]\}^{1/2} = |\det \mathbf{Q}_2(\mathbf{x}, \mathbf{x}')|^{1/2} = \mathcal{L}(\mathbf{x}, \mathbf{x}'),$$

cf. (Červený 2001, 4.10.11), can be identified as the relative geometrical spreading (see, for example, Aki & Richards 1980, 9.46 in the case of P waves). The matrix $\mathbf{Q}_2$ is a quantity, defined in (Červený 2001, 4.3.5), that can be computed numerically in a straightforward manner. We have

$$A(\mathbf{x}, \mathbf{x}') = \frac{1}{4\pi\,[\rho(\mathbf{x})V(\mathbf{x})\rho(\mathbf{x}')V(\mathbf{x}')]^{1/2}\,\mathcal{L}(\mathbf{x}, \mathbf{x}')}.$$

Similarly, we introduce the high-frequency Green's function for the case of a fluid region (in the absence of a solid region). Away from caustics at $\mathbf{x}$ and $\mathbf{x}'$, the Green's function is given by

$$G(\mathbf{x}, \mathbf{x}', t) = \frac{1}{\pi} \sum_m \mathrm{Re} \int_0^\infty B^{(m)}(\mathbf{x}, \mathbf{x}')\, \exp\{\mathrm{i}\omega\,[t - T^{(m)}(\mathbf{x}, \mathbf{x}')]\}\, \mathrm{d}\omega, \tag{8}$$

in which the amplitude $B^{(m)}$ is obtained from

$$B(\mathbf{x}, \mathbf{x}') = \frac{[\rho(\mathbf{x})\rho(\mathbf{x}')c_f(\mathbf{x})c_f(\mathbf{x}')]^{1/2}}{4\pi\,\mathcal{L}(\mathbf{x}, \mathbf{x}')}, \tag{9}$$

[with $c_f = (\sigma^{-1}\,\kappa)^{1/2}$ denoting the acoustic wave speed] upon, as above, multiplication of the phase factor that accounts for the KMAH index, *cf.* 5.1.7 with 5.1.60 and 5.1.48 of Červený (2001).

2.3 The source

The source is described by an equivalent body force, expressed in terms of the so-called symmetric stress glut tensor $\mathbf{S}$,

$$f_j = -\partial_i S_{ij}, \tag{10}$$

which, in turn, is related to the source moment tensor as

$$(\partial_{t_0} S_{ij})(\mathbf{x}_0, t_0) = M_{ij}\delta(\mathbf{x}_0 - \mathbf{x}^s)\delta(t_0 - t^s). \tag{11}$$

Substituting (10) into (11) gives

$$f_j(\mathbf{x}_0, t_0) = -M_{ij}\partial_i\delta(\mathbf{x}_0 - \mathbf{x}^s)\,H(t_0 - t^s), \tag{12}$$

where $H(t_0 - t^s)$ is the step function. For convenience, we shift t^s to 0 for each event.

Substituting (12) for the inhomogeneous right-hand side of the wave eq. (1), we obtain the asymptotic the solution,

$$u_i(\mathbf{x}, t) \simeq \frac{1}{\pi} \sum_m \text{Re} \int_0^\infty \xi_i(\mathbf{x}) \tfrac{1}{2}[\xi_p(\mathbf{x}^s)\gamma_q(\mathbf{x}^s) + \xi_q(\mathbf{x}^s)\gamma_p(\mathbf{x}^s)]\, M_{qp}$$
$$A^{(m)}(\mathbf{x}, \mathbf{x}^s)\,\exp\{i\omega\,[t - T^{(m)}(\mathbf{x}, \mathbf{x}^s)]\}\,d\omega, \tag{13}$$

in which

$$\gamma_p(\mathbf{x}^s) = (\partial_{s,p} T^{(m)})(\mathbf{x}, \mathbf{x}^s) \tag{14}$$

is the p-component of the slowness vector at $\mathbf{x}^s$ associated with the ray connecting $\mathbf{x}^s$ with $\mathbf{x}$. In the further construction, this will be the S wavefield incident upon the CMB.

Eq. (13) can be compared to (Aki & Richards 1980, 4.88–4.90) when we reduce the elastic stiffness to the isotropic elastic case with Lamé parameters λ and μ. In these equations, $M_{pq} = \mu\,(\bar{u}_p v_q + \bar{u}_q v_p)\,A$ in which v is the normal to the fault surface, $\bar{u}_p$ is the average displacement discontinuity and A is the fault area. Then the source radiation pattern can be written in the form

$$F(s) = \mathbf{M}^{-1}M_{qp}\xi_p(\mathbf{x}^s)\,V(\mathbf{x}^s)\gamma_q(\mathbf{x}^s),\quad \mathbf{M} = \mu A\|\bar{u}.$$

2.4 Background solid–fluid interface: the core–mantle boundary

The coefficients in the above equations are associated with a background model that is assumed to be smooth, except at an interface Σ such as the CMB. We couple the above expressions for propagation in the solid and fluid by imposing appropriate solid–fluid interface boundary conditions. Hereinafter, subscript F denotes parameters associated with the fluid, and the subscripts $+$ and $-$ refer to the fluid (core) and solid (mantle) side of Σ, respectively. The relevant aspects of the geometry are illustrated in Fig. 5.

First we consider the transmission from the mantle into the outer core, from S (in the solid) to K (in the fluid). We begin with the continuation equation for the displacement amplitude function (*cf.* Červený 2001, 5.4.4):

$$U(\mathbf{x}) = \left[\frac{\rho(\mathbf{x}')\|v(\mathbf{x}')\|}{\rho(\mathbf{x})\|v(\mathbf{x})\|}\right]^{1/2} \frac{\mathcal{L}(\mathbf{x}')}{\mathcal{L}(\mathbf{x})}\,U(\mathbf{x}'), \tag{15}$$

where $\mathcal{L}$ denotes geometrical spreading. The continuation equation for the pressure amplitude function is

$$P(\mathbf{x}) = \left[\frac{\rho_f(\mathbf{x})c_f(\mathbf{x})}{\rho_f(\mathbf{x}')c_f(\mathbf{x}')}\right]^{1/2} \frac{\mathcal{L}(\mathbf{x}')}{\mathcal{L}(\mathbf{x})}\,P(\mathbf{x}') \tag{16}$$

(*cf.* Červený 2001, 5.1.3). The spreading factors are purely geometrical and do not sense whether the wave is elastic or acoustic.
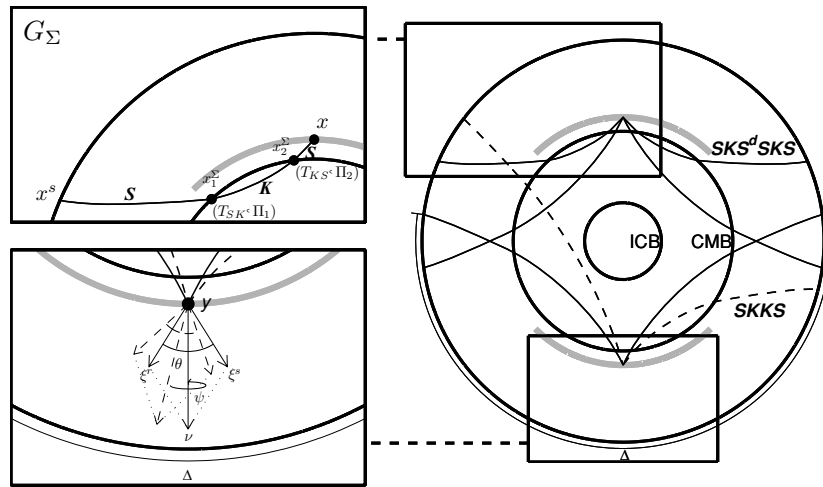

Figure 5. Schematic illustration of the path geometry of *SKKS* (right-hand side bottom) and *SKS^{d}SKS* (right-hand side top) considered in the generalized Radon transform (GRT) of *SKKS* data. The left-hand side two boxes are the blowups of the right-hand side boxes. Left-hand side top: At the CMB, (T_{SK}, Π_1) and (T_{KS}, Π_2) are calculated for positions x_1^Σ and x_2^Σ, respectively. Left-hand side bottom: The source and receiver are separated by epicentral distance Δ. The image point at the CMB is denoted by y. The sum of the slowness vectors of the two legs of *SKKS* is given by v. The scattering angle is θ and scattering azimuth is ψ. An image is, essentially, created by an integration over $v/\|v\|$, followed by an integration over (θ, ψ).

Let $\mathbf{x}_1^\Sigma$ denote the first point of refraction on Σ of the *SKS^{d}SKS* phase (Fig. 5). The transmission $\mathcal{T}_{KS}(\mathbf{x}_1^\Sigma)$ is governed by the expression

$$\mathcal{T}_{KS}\left(\mathbf{x}_1^\Sigma\right) = \frac{\left[\rho\left(\mathbf{x}_1^\Sigma\right)\|v\left(\mathbf{x}_1^\Sigma\right)\|\right]^{-1/2}}{\left[\rho_f\left(\mathbf{x}_1^\Sigma\right)c_f\left(\mathbf{x}_1^\Sigma\right)\right]_+^{1/2}} \frac{\mathcal{L}\left(\mathbf{x}_1^\Sigma\right)_+}{\mathcal{L}\left(\mathbf{x}_1^\Sigma\right)_-} T_{KS}\left(\mathbf{x}_1^\Sigma\right)\,, \tag{17}$$

in which T_{KS} is the plane-wave displacement-pressure transmission coefficient.

For the *K* wave, we get

$$P(\mathbf{x}) = \frac{[\rho_f(\mathbf{x})c_f(\mathbf{x})]^{1/2}}{[\rho(\mathbf{x}')\|v(\mathbf{x}')\|]^{-1/2}} \frac{\mathcal{L}(\mathbf{x}')}{\mathcal{L}(\mathbf{x})} \mathcal{T}_{KS}\left(\mathbf{x}_1^\Sigma\right) U(\mathbf{x}'), \tag{18}$$

in analogy with Červený (2001); 5.4.10 and 5.1.17.

Let $\mathbf{x}_2^\Sigma$ denote the second point of refraction on Σ of the *SKS^{d}SKS* phase (Fig. 5). This transmission is

$$\mathcal{T}_{SK}\left(\mathbf{x}_2^\Sigma\right) = \frac{\left[\rho_f\left(\mathbf{x}_2^\Sigma\right)c_f\left(\mathbf{x}_2^\Sigma\right)\right]_+^{1/2}}{\left[\rho\left(\mathbf{x}_2^\Sigma\right)\|v(\mathbf{x}_2^\Sigma)\|\right]_-^{-1/2}} \frac{\mathcal{L}\left(\mathbf{x}_2^\Sigma\right)_-}{\mathcal{L}\left(\mathbf{x}_2^\Sigma\right)_+} T_{SK}\left(\mathbf{x}_2^\Sigma\right), \tag{19}$$

so that the *S* wave directly illuminating the contrast in the lowermost mantle from the underside is represented by

$$U(\mathbf{x}) = \left[\frac{\rho(\mathbf{x}')\|v(\mathbf{x}')\|}{\rho(\mathbf{x})\|v(\mathbf{x})\|}\right]^{1/2} \frac{\mathcal{L}(\mathbf{x}')}{\mathcal{L}(\mathbf{x})} \mathcal{T}_{SK}\left(\mathbf{x}_2^\Sigma\right) \mathcal{T}_{KS}\left(\mathbf{x}_1^\Sigma\right) U(\mathbf{x}'). \tag{20}$$

To obtain a 'Green's tensor', we incorporate a point body-force source; then (20) attains the form

$$U(\mathbf{x}) = \left[\frac{\rho(\mathbf{x}')V(\mathbf{x}')}{\rho(\mathbf{x})V(\mathbf{x})}\right]^{1/2} \frac{1}{\mathcal{L}(\mathbf{x},\mathbf{x}')} \mathcal{T}_{SK}\left(\mathbf{x}_2^\Sigma\right) \mathcal{T}_{KS}\left(\mathbf{x}_1^\Sigma\right) \frac{1}{4\pi\rho(\mathbf{x}')V(\mathbf{x}')} =: C(\mathbf{x},\mathbf{x}'). \tag{21}$$

In this expression, the relative geometrical spreading

$$\mathcal{L}\left(\mathbf{x},\mathbf{x}'\right) = \left|\det\left[\mathbf{Q}_2\left(\mathbf{x},\mathbf{x}_2^\Sigma\right)\mathbf{\Pi}_2\mathbf{Q}_2\left(\mathbf{x}_2^\Sigma,\mathbf{x}_1^\Sigma\right)\mathbf{\Pi}_1\mathbf{Q}_2\left(\mathbf{x}_1^\Sigma,\mathbf{x}'\right)\right]\right|^{1/2} \tag{22}$$

includes the effect of CMB curvature on the transmission from mantle to core $\mathbf{\Pi}$ (*cf.* Červený 2001, 4.14.71)

$$\mathbf{\Pi}_1 = \left(\mathbf{G}_+ - \mathbf{A}_+^{\mathrm{an}}\right)^{-1}\mathbf{M}^{\mathrm{F}}\left(\mathbf{x},\mathbf{x}_1^\Sigma,\mathbf{x}'\right)\left[(\mathbf{G}_- - \mathbf{A}_-^{\mathrm{an}})^{-1}\right]^T. \tag{23}$$

Here, $\mathbf{M}^{\mathrm{F}}$ is the Fresnel zone matrix at $\mathbf{x}_1^\Sigma$ and $\mathbf{A}_+^{\mathrm{an}} = \mathbf{0}$; $\mathbf{G}$ is the transformation matrix defined in Červený (2001), 4.4.12. A similar expression is obtained for $\mathbf{\Pi}_2$ from the outer core back into the lowermost mantle. The associated traveltime is given by

$$T_\Sigma\left(\mathbf{x},\mathbf{x}'\right) = T\left(\mathbf{x},\mathbf{x}_2^\Sigma\right) + T\left(\mathbf{x}_2^\Sigma,\mathbf{x}_1^\Sigma\right) + T\left(\mathbf{x}_1^\Sigma,\mathbf{x}'\right). \tag{24}$$

With (21) and (24), the 'Green's tensor' associated with an *SKS* leg follows to be of the form

$$G_{ip}^\Sigma(\mathbf{x},\mathbf{x}',t) = \frac{1}{\pi}\,\mathrm{Re}\int_0^\infty \xi_i(\mathbf{x})\xi_p(\mathbf{x}')C^{(m)}(\mathbf{x},\mathbf{x}')\exp\left\{\mathrm{i}\omega\left[t - T_\Sigma^{(m)}(\mathbf{x},\mathbf{x}')\right]\right\}\,\mathrm{d}\omega \tag{25}$$

(compare 5). As before, *C* is obtained by accounting for the KMAH index.

2.5 The short-period Born approximation and inverse scattering

In the previous subsection, we obtained the asymptotic Green's tensors, G_{ip}^Σ, for wave propagation (*SKS*) in a background model which is generally smooth but which contains a (known and fixed) interface at the CMB. We now describe the scattered wavefield, that is *SKS^{d}SKS* phase, in terms of the medium contrasts (in the lowermost mantle) relative to this background. Let $\mathbf{x}^s$ denote a source location, as before, and $\mathbf{x}^r$ a station location; $\mathbf{y}$ denotes a scattering point, see Fig. 5. To obtain the scattered displacement, we substitute $G_{kq}^\Sigma(\mathbf{y},\mathbf{x}^s)$ and $G_{pi}^\Sigma(\mathbf{x}^r,\mathbf{y})$ for the source and receiver Green's tensors, respectively, in the Born approximation for *SKS^{d}SKS* (Burridge *et al.* 1998. (2.20)).

The two-way traveltime for the *SKS^{d}SKS* phase is the sum,

$$T(\mathbf{x}^s,\mathbf{x}^r,\mathbf{y}) = T_\Sigma(\mathbf{y},\mathbf{x}^s) + T_\Sigma(\mathbf{x}^r,\mathbf{y})\,. \tag{26}$$

We denote quantities associated with a (*SKS*) ray connecting the scattering point $\mathbf{y}$ with an earthquake location $\mathbf{x}^s$ by a superscript *s* and the quantities associated with a (*SKS*) ray connecting the scattering point $\mathbf{y}$ with a station at $\mathbf{x}^r$ by a superscript *r*. The relative medium contrast, representing the scatterers in the lowermost mantle, is described by

$$\mathbf{c}^{(1)}(\mathbf{y}) = \left\{\frac{\rho^{(1)}(\mathbf{y})}{\rho(\mathbf{y})}, \frac{c_{ijk\ell}^{(1)}(\mathbf{y})}{\rho(\mathbf{y})V_\circ^s(\mathbf{y})V_\circ^r(\mathbf{y})}\right\}, \tag{27}$$

where $V_\circ^s$ is the local phase velocity of the 'incident' $(SKS)^s$ mode, averaged over all phase directions, whereas $V_\circ^r$ is the local phase velocity of the 'scattered' $(SKS)^r$ mode, averaged over all phase directions. The contrast-source radiation patterns are given by

$$\mathbf{w}(\mathbf{x}^s,\mathbf{x}^r,\mathbf{y}) = \left\{\xi^s(\mathbf{y})\xi^r(\mathbf{y}), V_\circ^s(\mathbf{y})V_\circ^r(\mathbf{y})\left[\xi_i^s(\mathbf{y})\gamma_j^s(\mathbf{y})\xi_k^r(\mathbf{y})\gamma_\ell^r(\mathbf{y})\right]\right\}, \tag{28}$$

and the source radiation pattern is captured by the quantity (*cf.* 13)

$$W(\mathbf{x}^s,\mathbf{x}^r,\mathbf{y}) = M_{qr}(\mathbf{x}^s)\tfrac{1}{2}[\xi_q^s(\mathbf{x}^s)\gamma_r^s(\mathbf{x}^s) + \xi_r^s(\mathbf{x}^s)\gamma_q^s(\mathbf{x}^s)] = \mathbf{M}(\mathbf{x}^s)V(\mathbf{x}^s)^{-1}F(\mathbf{x}^s). \tag{29}$$

We obtain the short-period Born approximation for the scattered displacement $u_p^{(1)}$ [here, $m = (m^s, m^r)$]:

$$u_p^{(1)}(\mathbf{x}^s, \mathbf{x}^r, t) = -\frac{1}{\pi} \operatorname{Re} \int_0^\infty \int (-\omega^2) W(\mathbf{x}^s, \mathbf{x}^r, \mathbf{y}) \xi_p^r(\mathbf{x}^r) \rho(\mathbf{y})$$
$$\times C^{(r)}(\mathbf{x}^r, \mathbf{y}) C^{(s)}(\mathbf{y}, \mathbf{x}^s) \mathbf{w}^T(\mathbf{x}^s, \mathbf{x}^r, \mathbf{y}) \mathbf{c}^{(1)}(\mathbf{y}) \exp\{i\omega[t - T(\mathbf{x}^s, \mathbf{x}^r, \mathbf{y})]\} \, dV(\mathbf{y}) \, d\omega. \tag{30}$$

This result defines a linear integral operator, $\mathcal{F}$, by identifying $u^{(1)} = \mathcal{F} \mathbf{c}^{(1)}$. The inverse scattering transform is then determined by forming $(\mathcal{F}^* \mathcal{F})^{-1} \mathcal{F}^*$, where the imaging operator, $\mathcal{F}^*$, is the adjoint of $\mathcal{F}$. The construction of the inverse scattering transform follows closely the procedure developed in De Hoop & Brandsberg-Dahl (2000) and is not repeated here. The construction can be carried out for image points $\mathbf{y}$ locally in D'' proper. For the practical implementation, we rely on the fact that the angle of incidence and the angle of refraction from S to K or K to S are close to one another.

In our current implementation, we evaluate the traveltime functions $T_\Sigma(\mathbf{y}, \mathbf{x}^s)$ and $T_\Sigma(\mathbf{x}^r, \mathbf{y})$ in (26) by using the 3-D velocity model by Grand (2002) and first-order perturbation theory. With the knowledge of R_{KK} at the CMB, we use the $SKKS$ phase to estimate $W(\mathbf{x}^s, \mathbf{x}^r, \mathbf{y})$ in (29) and the illumination footprint, based on the 'GRT' intercepted in the outer core using (18) instead of (20). Here, we approximate the points $\mathbf{x}_2^\Sigma$ by the bounce point of $SKKS$.

3 RESOLUTION AND MULTIPLE SUPPRESSION

We test the performance of the approach developed above with synthetic $SKS^d SKS$ computed with WKBJ (Chapman 1978) using the radially stratified wave speed model *ak135* (Kennett *et al.* 1995). For the calculation of the waveforms, we superimpose jumps in elastic parameters at certain distances above the CMB. The seismograms in Fig. 6(a) are calculated from a model with a 3 per cent wave-speed increase at 250 km above the CMB. The phases in the shaded area are the multiples, $SK_N S$, which reflect at the CMB $N - 1$ times. The traveltime curve (dashed lines in Fig. 6) of underside reflections from a D'' at a typical depth (150–350 km above the CMB) intercepts with the multiples (see Fig. 6).

$SKKS$ and $SKS^d SKS$ are so-called min–max (or mixed) phases, and their waveforms are subjected to a $\pi/2$ phase shift (in accordance with the caustic surface depicted in the outer core in Fig. 1b; see Fig. 6a). The KMAH index can be applied and compensated for, with a Hilbert transform, but it is more straightforward to deconvolve the phases by themselves. To achieve this we follow the procedure developed in Wang *et al.* (2006). That is, after aligning the synthetic data (using multichannel cross correlation, MCCC), we use a principal component analysis (PCA) to estimate the $SKKS$ phase; we then deconvolve this estimation from the full synthetic seismograms. The resulting seismograms (after deconvolution) are shown in Fig. 6(b).

From the synthetic data we produce GRT common image point gathers, that is, radial profiles of elasticity contrasts for the same image point but for different scattering (opening) angles (Fig. 8). Presumably, any (real) reflector should show up at (or close to) the same radius in a common image point gather for any processed scatter angle θ (having integrated over azimuths ψ). The final reflectivity profiles—that is, the GRT images either produced by integration (Wang *et al.* 2006) over scattering angle or estimated by statistical inference (Ma *et al.* 2007)—are shown on the right-hand side.

For the wave-speed model and associated ray geometries considered, we calculate—as a function of scatter angle—the (linearized) SS reflection coefficient associated with $SKS^d SKS$. In Fig. 7, we illustrate how well we can resolve this reflection coefficient using the 'GRT' generated image gathers, also with the uneven distribution of source–receiver pairs in the data study presented in the next section. Since the main purpose here is to test the correctness of the GRT code, to avoid the interface of multiples to the amplitude at the D'', we do not include the multiples in our synthetic seismic data.

The multiples $SK_N S$ form a series of events with approximately parabolic moveouts in the angle gathers (Fig. 8a). The GRT image on the right-hand side indicates that these multiples do not interfere with reflections from lowermost mantle interfaces (such as the presumed top of D'') more than 200 km above the CMB. But signal from scatterers closer to the CMB may be contaminated by $SK_N S$ arrivals. If one
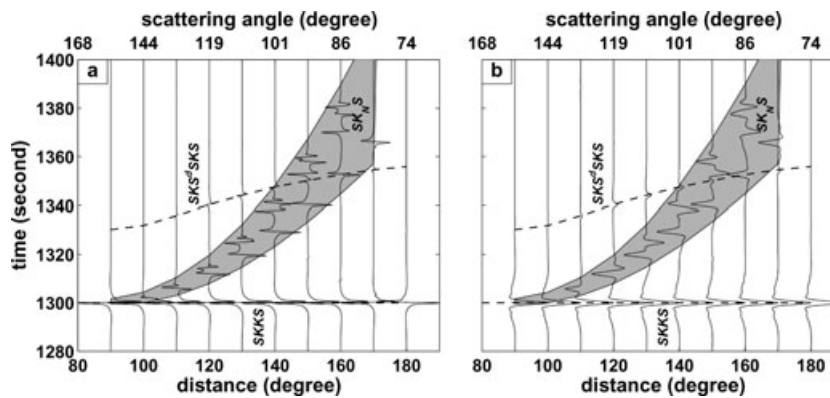

Figure 6. (a) Record section of synthetic data for a model with one contrast which is 250 km above the CMB, calculated with the WKBJ method. The record section is aligned by $SKKS$ phase. The phases in the shading window are multiples $SK_N S$. The red dashed line is the traveltime curve of $SKS^d SKS$ phases. (b) Record section of synthetic data deconvolved by the PCA estimated $SKKS$ phase.
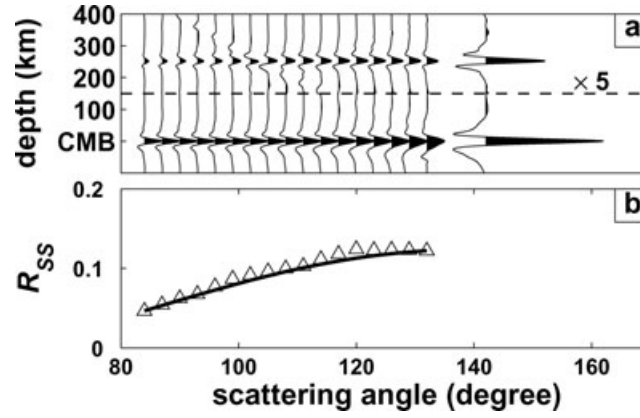
Figure 7. Illustration of the reconstruction of the linearized reflection coefficient 250 km above the CMB from the WKBJ synthetics using the 'GRT'.
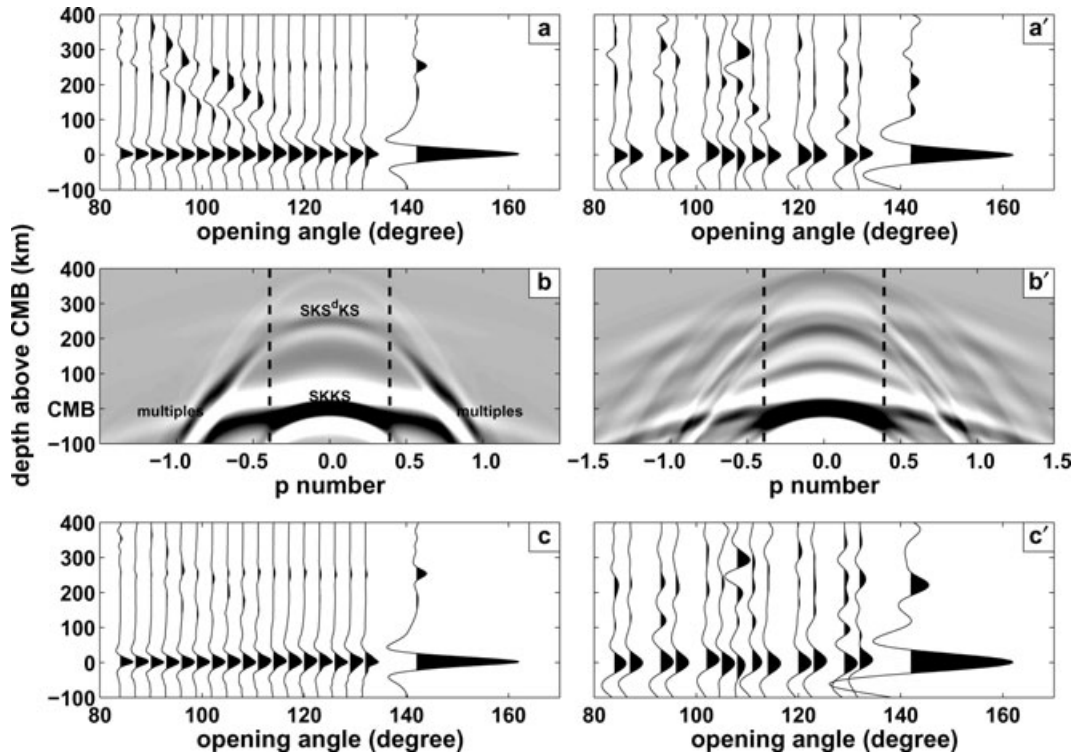

Figure 8. Illustration of the act of parabolic Radon transform for both synthetic (left-hand side) and real (right-hand side) data. (a)/(a′), angle gathers with multiples; (b)/(b′), parabolic Radon transform of (a)/(a′); (c)/(c′), angle gathers after the removal of multiples.

would know the exact arrivals of the interfering phases, one could suppress them with a simple mute in the data domain. Such a mute should be avoided, however. First, it also removes SKS^dSKS arrivals in the chosen time-distance window. Second, and more fundamental, one does not know *a priori* the arrival of interfering phases so that one would need to choose the mute windows conservatively and thus, instead to retain as much SKS^dSKS signal as possible, we remove the interfering phases using information gleaned from the angle gathers. This involves three steps: (1) angle gathers are obtained by applying a GRT to the seismic data (see Fig. 8a); (2) a parabolic Radon transform is applied to the angle gathers and the energy corresponding to mulitples was identified (the area outside the dashed lines); (3) an inverse parabolic Radon transform is then applied to the outside area ($\|p\| > 0.4$). The output was subtracted from the angle gathers in Fig. 8(a). In Fig. 8(c), we show the angle gathers where the multiples have been attenuated (but SKS^dSKS signal preserved). Indeed, by methods of parabolic Radon transform, we succeed in attenuating the multiples.

4 PROOF OF CONCEPT—IMAGING THE CMB REGION WITH *SKKS* WAVES

Through comparison with results of the GRT imaging with *ScS* (Wang *et al.* 2006) we demonstrate here that inverse scattering of the broad-band *SKKS* wavefield can indeed be used to constrain interfaces in the vicinity of the CMB (that is, within D″). As a proof-of-concept

we present results for the CMB beneath Central America, a region that has been studied intensively (Buffett *et al.* 2000; Garnero 2000; Thomas *et al.* 2004; Van der Hilst *et al.* 2007).

4.1 Data selection and pre-processing

Fig. 9 depicts the distribution of ∼38 000 (specular) *SKKS* reflection points at the underside of the CMB in the same 50° × 50° patch as studied in Wang *et al.* (2006) and Van der Hilst *et al.* (2007). The *SKKS* data coverage, produced by ∼2200 earthquakes (blue stars) that are recorded at one or more of a total of ∼1000 stations (inverted red triangles) is much more even than the distribution of *ScS* bounce points in the same region.

For each event, origin times and hypocentre locations are obtained from the catalogue produced by Engdahl *et al.* (1998), hereinafter referred to as EHB data. The three-component, broad-band waveforms are obtained from the data management centre of the Incorporated Research Institutions for Seismology (IRIS). The minimum magnitude considered in this study is $m_b \geq 5.1$. The range of (angular) epicentral distances was set at $100°-180°$ to avoid contamination with SKP^dPKS.

We follow the data pre-processing sequence of Wang *et al.* (2006), with *SKKS* instead of *ScS* as the reference phase for the principal component analysis (PCA). The bandpass filter used here is 10–50 s. The final image traces are inferred (using appropriate weights) from the image gathers at different opening angles θ (after integration over scattering azimuth ψ). Prior to 'stacking' each of the gathers (or, as we do here, statistical inference) we correct the traveltime using Grand's 3-D mantle model for shear wave speed (Grand 2002). As explained in the previous section, we suppress the interference of higher-order multiples (SK_NS, $N > 2$) using a parabolic Radon transform.

4.2 Preliminary results

To illustrate the concepts developed so far, we first construct GRT image gathers for three locations along CMB profile $B-B'$ in Van der Hilst *et al.* (2007), see the inset in Fig. 9. In Figs 10(a)–(c), the 17 traces on the left-hand side are the common image point gathers for *SKKS* as a function of scattering (opening) angle. We note that, unlike S_dS, which changes polarity at the intramission angle, SKS^dSKS keeps the same polarity. The two traces on the right-hand side are reflectivity profiles obtained from *SKKS*, that is, from the image gathers on the left-hand side, and from *ScS* (following procedures in Wang *et al.* 2006; Ma *et al.* 2007). We note that the *ScS* images were constructed from data bandpassed between 1–50 s (as opposed to 10–50 s for *SKKS*).

Although there are slight differences, both the *SKKS* and the *ScS* images suggest the presence of a distinct reflector between 200 and 300 km above the CMB. These signals correspond to interface $L1$, which Van der Hilst *et al.* (2007) interpreted as the top D'' discontinuity and, presumably, the location of the post-perovskite (ppv) transformation. The *SKKS* and *ScS* images also present pulses associated with a wave-speed decrease closer to the CMB. These could mark the interface $L2$, which Van der Hilst *et al.* (2007) interpreted as the base of the ppv lens (see fig. 3 in Van der Hilst *et al.* 2007). However, for the frequencies considered, this $L2$ structure is within the side lobe of the *SKKS* CMB reflection (Fig. 10b).

Juxtaposition of radial reflectivity profiles produces 2-D seismic sections. Fig. 11 presents image profiles along section $B-B'$ discussed by Van der Hilst *et al.* (2007) (their fig. 3B) both for *ScS* and *SKKS*. To obtain these results, the data were inverted separately, so that the *ScS* and *SKKS* image profiles are, indeed, entirely independent. There are differences, but there is substantial similarity in the images of the major
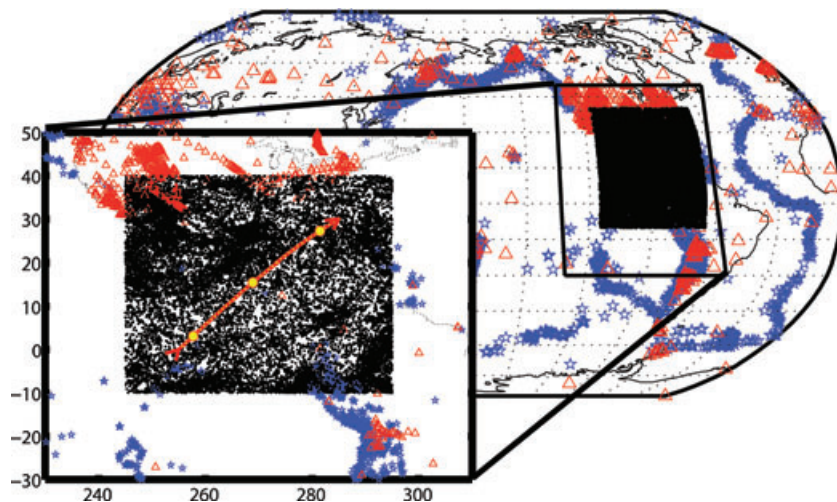

Figure 9. Geographic map of the region under study, depicting the epicentres of the ∼2200 earthquakes (blue stars) and the locations of the ∼1000 stations (inverted red triangles) that yielded the data used in the construction of the common image-point gathers. The 50° × 50° CMB bin is indicated by the densely sampled rectangle: small black dots mark specular CMB reflection points of the ∼38 000 *SKKS* records. The inset in the left-hand side is the blowup of the black block on the right-hand side. The red arrow points along the $B-B'$ profile in fig. 1 by Van der Hilst *et al.* (2007). The angle gathers at the three yellow dots, from left- to right-hand side, are shown in Figs 10(a), (c) and (b), respectively.
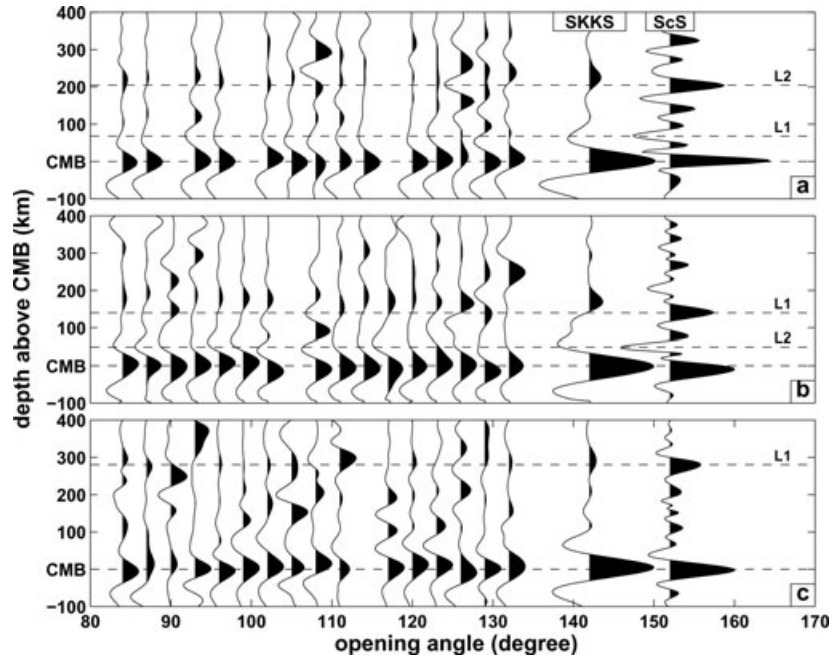
Figure 10. Illustration of angle gathers and radial image traces with real data for three CMB locations marked in the blowup in Fig. 9. *L*1 and *L*2 follow the meaning in Van der Hilst *et al.* (2007). The right-hand side two traces are the image estimates from *SKKS* data and *ScS* data (from fig. 3B in Van der Hilst *et al.* 2007).
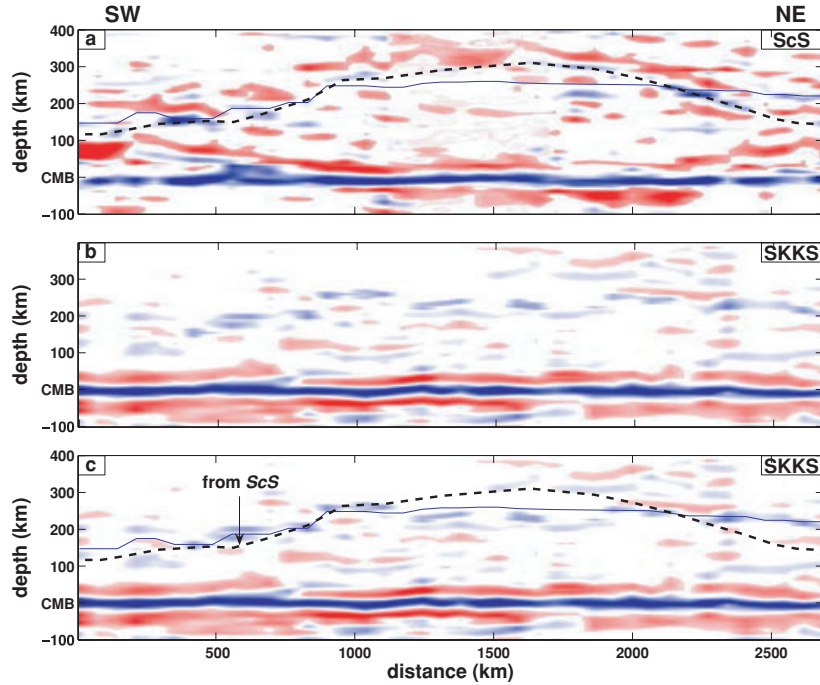

Figure 11. Comparison of image sections obtained using a generalized Radon transform of *ScS* (a) and *SKKS* data (from fig. 3B in Van der Hilst *et al.* 2007). The solid blue line in (a) is the *D″* elevation predicted by Sidorin *et al.* (1999). The dashed black lines in (a) and (c) are the observed *D″* from *ScS* transform.

features (in particular, the CMB and top *D″*) are in excellent agreement with each other. To illustrate the latter, in Fig. 11(c), the dashed line depicts the top *D″* interface inferred from the *ScS* result (Fig. 11a). We note that these preliminary *SKKS* images do not reveal the concave up *L*2 interface that is visible in the *ScS* image.

5 DISCUSSION AND CONCLUDING REMARKS

Changes in elastic parameters in the lowermost mantle have been the subject of many seismological studies (Lay & Helmberger 1983; Sidorin *et al.* 1999; Garnero 2000; Thomas *et al.* 2004; Hutko *et al.* 2006), and GRT imaging with broad-band *ScS* data, as introduced by Wang

et al. (2006), has begun to enable large-scale exploration of structure near the CMB (Van der Hilst *et al.* 2007). However, due to the uneven distribution of *ScS* midpoints, many regions are beyond the reach of GRT imaging with *ScS* data alone.

We demonstrate here the feasibility of GRT-type inverse scattering of the *SKKS* wavefield and its coda, which samples the D'' region from below (i.e. from the core side). For this purpose, we developed an imaging operator that can detect contrasts relative to a background medium that itself contains a (known) interface (but is otherwise smooth). Formally speaking, such an operator is not a GRT, but because the wave speed contrast associated with the K to S refraction at the CMB is small, the properties of the mentioned imaging operator are close to those of a GRT. In the space–time domain, higher-order multiples can interfere with underside reflections at D'' structure, but with parabolic Radon transform methods applied to angle gathers their contributions can be attenuated. We note, however, that because of the difference in slowness, the contribution of SK_NS ($N > 2$) to the GRT images is small even without this additional processing step.

We illustrate the method with an application to *SKKS* data associated with midpoints beneath Central America. The (preliminary) image gathers detect a strong contrast at a depth coinciding with the CMB—this merely provides a consistency check for the background Green's functions. The inferred structures above the CMB are remarkably consistent with the results of GRT imaging with broad-band *ScS* data (Wang *et al.* 2006; Van der Hilst *et al.* 2007), even though two completely independent data sets were used. Indeed, the polarization (*SH* versus *SV*), propagation path geometry (top versus bottom reflection), the source–receiver pairs and the time windows extracted from the seismograms are entirely different.

These preliminary results are promising and suggest that imaging with the *SKKS* wavefield represents a viable alternative and complement to imaging with *ScS* waves. The *SKKS* midpoint distribution is much more than that of even *ScS*. Fig. 2 indicates that one may be able to use *SKKS* to constrain the D'' region—at least the interface that marks the top of D''—on a hemisphere scale from Eurasia, across Japan, the Pacific, the Americas into the Atlantic. Furthermore, in areas that are well sampled by both *ScS* and *SKKS*, such as the lowermost mantle beneath Central America and East Asia, joint *ScS*–*SKKS* inversion could produce superior images of D'' structure. For this purpose, *ScS* and *SKKS* can be combined to form a GRT integration over migration dip directions covering the entire (unit) sphere. However, one should do such integration with caution. Whereas the major interfaces observed with *ScS* and *SKKS* are consistent with each other (Figs 10 and 11), there are differences that need to be fully understood before a rigorous and meaningful joint interpretation can be undertaken. For instance, the different sensitivity of *ScS* (*SH*) and *SKKS* (*SV*) waves to (radial) anisotropy could be a challenge and an opportunity.

REFERENCES

Aki, K. & Richards, P.G., 1980. *Quantitative Seismology: Theory and Methods*, **Vol. 1**, Freeman, San Francisco.

Alvarez, G. & Larner, K., 2004. Relative performance of moveout-based multiple-suppression methods for amplitude variation with offset (avo) analysis and common midpoint (cmp) stacking, *Geophysics*, **69**, 275–285.

Beylkin, K., 1984. The inversion problem and applications of the generalized Radon transform, *Comm. Pure Appl. Math.*, **37**, 579–599.

Buffett, B.A., Garnero, E.J. & Jeanloz, R., 2000. Sediments at the top of the Earth's core, *Science*, **290**, 1338–1342.

Burridge, R., de Hoop, M.V., Miller, D. & Spencer, C., 1998. Multiparameter inversion in anisotropic media, *Geophys. J. Int.*, **134**, 757–777.

Červený, V., 2001. *Seismic Ray Theory*, Cambridge University Press, Cambridge.

Chambers, K. & Woodhouse, J., 2006. Investigating the lowermost mantle using migrations of long-period *S-ScS* data, *Geophys. J. Int.*, **166**, 667–678.

Chapman, C.H., 1978. New method for computing synthetic seismograms, *Geophys. J. Int.*, **54**, 481–518.

Clitheroe, G. & Van der Hilst, R.D., 1998. Complex anisotropy in the Australian lithosphere from shear-wave splitting in broad-band *SKS* records, in *Structure and Evolution of the Australian Continent*: Geodynamics Series, Vol. 26, pp. 73–78, Braun, J., Dooley, J., Goleby, B., van der Hilst, R. and Klootwijk, C., American Geophysical Union, Washington, DC.

De Hoop, M.V. & Brandsberg-Dahl, S., 2000. Maslov asymptotic extension of generalized radon transform inversion in anisotropic elastic media: a least-squares approach, *Inv. Prob.*, **16**, 519–562.

Engdahl, E.R., van der Hilst, R.D. & Buland, R.P., 1998. Global teleseismic earthquake relocation from improved travel times and procedures for depth determination, *Bull. seism. Soc. Am.*, **88**(3), 722–743.

Garnero, E.J., 2000. Heterogeneity of the lowermost mantle, *Ann. Rev. Earth Planet. Sci.*, **28**, 509–537.

Grand, S.P., 2002. Mantle shear-wave tomography and the fate of subducted slabs, *Phil. Trans. Roy. Soc., A,* **360**, 2475–2491.

Hutko, A.R., Lay, T., Garnero, E.J. & Revenaugh, J., 2006. Seismic detection of folded, subducted lithosphere at the core-mantle boundary, *Nature*, **441**, 333–336, doi:10.1038/nature04757.

Kennett, B.L.N., Engdahl, E.R. & Buland, R.P., 1995. Constraints on seismic velocities in the Earth from travel times, *Geophys. J. Int.*, **122**, 108–124.

Lay, T. & Helmberger, D.V., 1983. A shear velocity discontinuity in the lower mantle, *Geophys. Res. Lett.*, **10**, 63–66.

Ma, P., Wang, P., de Hoop, M.V., Tenorio, L. & van der Hilst, R.D., 2007. Imaging of structure at and near the core mantle boundary using a generalized Radon transform II: statistical inference of singularities, *J. geophys. Res.*, **112**, B08303, doi:10.1029/2006JB004513.

Romanowicz, B., 2003. Global mantle tomography: progress status in the past 10 years, *Ann. Rev. Earth Planet. Sci.*, **31**, 303–328.

Rost, S. & Revenaugh, J., 2004. Small-scale changes of core–mantle boundary reflectivity studied using core reflected *PcP*, *Phys. Earth planet. Inter.*, **145**, 19–36.

Sidorin, I., Gurnis, M. & Helmberger, D.V., 1999. Evidence for a ubiquitous seismic discontinuity at the base of the mantle, *Science*, **286**, 1326–1331.

Sze, E. & van der Hilst, R.D., 2003. Core mantle boundary topography from short period *PcP*, *PKP*, and *PKKP* data, *Phys. Earth planet. Inter.*, **135**, 27–46.

Thomas, C., Garnero, E.J. & Lay, T., 2004. High-resolution imaging of lowermost mantle structure under the Cocos plate, *J. geophys. Res.*, **109**, B08307.

Van der Hilst, R.D., Widyantoro, S. & Engdahl, E.R., 1997. Evidence for deep mantle circulation from global tomography, *Nature*, **386**, 578–584.

Van der Hilst, R.D., de Hoop, M.V., Wang, P., Shim, S.-H., Ma, P. & Tenorio, L., 2007. Seismo-stratigraphy and thermal structure of Earth's core–mantle boundary region, *Science*, **315**, 1813–1817.

Wang, P., de Hoop, M.V., van der Hilst, R.D., Ma, P. & Tenorio, L., 2006. Imaging of structure at and near the core mantle boundary using a generalized Radon transform I: construction of image gathers, *J. geophys. Res.*, **111**, B1230, doi:10.1029/2005JB004241.